Simulations of shear-induced melting and ordering

Mark J. Stevens
Corporate Research Science Laboratories, Exxon Research and Engineering Co., Annandale, New Jersey 08801

Mark O. Robbins
Department of Physics and Astronomy, The Johns Hopkins University, Baltimore, Maryland 21218
(Received 18 May 1993; revised manuscript received 29 July 1993)

We describe the effect of shear on the solid-liquid phase boundary of particles that interact via a screened Coulomb potential. Both fcc and bcc phases shear through layer-over-layer sliding. As the shear rate $\dot{\gamma}$ increases from zero, the degree of disorder in the layers increases and the stacking sequence changes. A first-order shear-melting transition occurs if the temperature is greater than about half of the equilibrium melting temperature T_m^{eq}. Near T_m^{eq} the transition rate is proportional to $T_m^{eq} - T$. As $\dot{\gamma}$ increases further, shear becomes an ordering influence and a reentrant solid phase is observed. Dimensionless plots of the nonequilibrium phase diagram and of the shear stress versus strain rate show considerable universality and are in excellent agreement with experiments on charge-stabilized colloidal suspensions.

PACS number(s): 62.20.−x, 64.70.Dv, 82.70.Dd

I. INTRODUCTION

There has been growing interest in the effect of shear on the structure and dynamics of condensed matter. Several types of shear-induced phase transitions have been discovered, including shear-induced melting [1–15], shear-induced ordering [11–27], phase segregation [28], and liquid-crystal transitions [29–31]. These transitions are of fundamental interest as examples of nonequilibrium phase transitions, and may aid the construction of general criteria for identifying stable steady states far from equilibrium. Studies of the mechanism of shear flow and the structure of shearing systems are also of great practical interest. Shear can be used to produce desired alignments of a system or to change its phase. An understanding of solid flow at high shear stresses is needed for models of flow in the Earth's crust [32] and of friction and wear [33].

In this paper we consider the effect of shear on the relatively simple phases formed by spherical particles interacting with a purely repulsive screened Coulomb (Yukawa) potential. The potential and parameters are chosen to correspond to a well-studied experimental system—charge-stabilized colloidal suspensions of spherical particles. These systems have several features which make them particularly fruitful testing grounds for theory and experiment. One is that their interactions are fairly simple [34], and can be varied continuously by changing the density of particles or by adding salt to the solution (see Sec. II). A second is that colloidal spheres form fcc, bcc, and fluid phases like atomic matter, but with interparticle separations of 1 μm rather than 0.1 nm [14,35–41]. The large separation allows the structure of suspensions to be imaged directly with light. It also leads to dramatic reductions in the elastic moduli, which scale as energy per unit volume. Since the energy scale in colloidal solids is comparable to that in atomic solids, the elastic moduli are roughly 10^{-12} times weaker than in atomic systems [42]. This makes it possible to study the response of systems at extremely high dimensionless shear stresses with a benchtop experiment.

Experimental studies of charge-stabilized colloidal suspensions have focused on measurements of the shear stress [42–44] σ and structure factor [1,3] $S(k)$ as a function of shear rate $\dot{\gamma}$. At low shear rates, polycrystalline samples become aligned in an orientation which minimizes the shear stress. As $\dot{\gamma}$ increases, gradual structural transformations occur [1–3]. In some cases, these culminate in a first-order melting transition [1,3,42,43], while other suspensions remain solid [15]. Normalized values of the stress vs strain-rate for different systems fall onto nearly universal solid and fluid curves. A counterintuitive observation is that the measured shear stress *increases* discontinuously when the solid melts—solids with the preferred alignment flow more easily (are less viscous) than fluids [42,43].

In this paper, we present detailed calculations of the nonequilibrium phase diagram, structure, and shear stress of systems whose equilibrium phase is fcc, bcc, or fluid. The main mechanism of shear in solid phases is shown to be layer-over-layer sliding. The calculated stress vs strain-rate curves are in good quantitative agreement with experiments, and show the same universal solid and fluid behavior. A dimensionless shear-melting phase diagram is constructed, and found to agree with most existing experimental data. Shear plays a surprising dual role in this phase diagram. Low shear rates increase the degree of disorder and destabilize the solid phase. Sufficiently high shear rates increase the degree of *order* and lead to a reentrant solid phase [14].

We also compare our results to previous simulations and to analytic calculations. Analytic work has treated shear as a weak perturbation from equilibrium within a density-functional or mode-coupling theory [7–9]. Ramaswamy and Renn [8] and Bagchi and Thirumalai [9]

concluded that the shear-melting transition evolved continuously from equilibrium melting, and that the transition point decreased as $\dot{\gamma}^2$. Our simulations support the view that shear-melting evolves continuously from the equilibrium transition. However, we find that the leading correction scales linearly with $\dot{\gamma}$ and show that this can be attributed to the presence of a finite yield stress for the solid phase.

Most simulations have focused on structural changes within sheared fluids [11,16,22–25,27,45]. Several groups have found an ordered phase at high shear rates which is closely related to our reentrant solid. However, we find strong two-dimensional order within shearing planes of atoms while some previous groups [11,27] have identified one-dimensional "stringlike" order along the velocity direction. The presence of an ordered phase at high shear rates remains controversial [20,24,25], and we discuss what facets of an experiment or calculation may influence its existence.

Prior to our recent work with Yukawa potentials [14], the effect of shear on solid phases had only been studied for the case of a soft sphere potential [5,46]. Evans [5] found a melting transition, but without the stress discontinuity seen in experiments [42,43]. As pointed out by Brown and Clarke [46], this may be because the system was not sheared in the experimentally observed crystal alignment. Brown and Clarke performed constant-stress simulations of fcc crystals in the observed alignment [46]. As in our simulations, the solid sheared through plane-over-plane sliding and the stacking of planes changed with shear rate. However, they did not observe shear-melting in their system.

The outline of the rest of the paper is as follows. Section II describes the interactions between charged colloidal spheres and the characteristic time scales for their motion. Details of our simulation techniques are provided in Sec. III. Then results for the changes in the orientation, phase, stress and structure of sheared systems are presented in Sec. IV. Concluding remarks and a summary are given in Sec. V.

II. PHYSICAL PARAMETERS

A. Interparticle potential

The Derjaguin-Landau-Verwey-Overbeek (DLVO) potential [34,47] provides a very successful description of interactions between like-charged spheres in solution. The potential contains a screened Coulomb repulsion and a van der Waals attraction. The latter is negligible in the systems of interest here. Although the original derivation of the DLVO potential is only valid for weakly charged spheres and low volume fractions, analytic [48] and numerical studies [49] show that it can be used more generally. However, the bare charge Z must be replaced by a smaller effective or "renormalized" charge Z^*. The pair potential for spheres of radius R and density ρ is then a Yukawa potential:

$$u(r) = U_0 \frac{e^{-\kappa r}}{r}, \tag{2.1}$$

where

$$\kappa^2 = \frac{4\pi e^2}{\epsilon k_B T}(Z^*\rho + 2\rho_s), \tag{2.2}$$

$$U_0 = \frac{(Z^*e)^2}{\epsilon}\frac{e^{2\kappa R}}{(1+\kappa R)^2}, \tag{2.3}$$

ϵ is the dielectric constant of the solvent, T is the temperature, and ρ_s is the molecular density of added salt (typically HCl in experiments). We will use the typical interparticle spacing $a = \rho^{-1/3}$ to make lengths dimensionless.

The experimentally controlled parameters are ρ_s and the volume fraction of spheres, $\phi = 4\pi R^3\rho/3$. Figure 1 shows the calculated equilibrium phase diagram [41] for spheres with $R = 455$ Å and $Z^* = 450$ in water at $T = 300$ K where $\epsilon = 78$. The phase diagram is typical of that found for many other sets of parameters in experiments and calculations [50]. Three phases are evident: a fluid phase and bcc and fcc solid phases. As ρ_s increases from zero, the Coulomb repulsion becomes more strongly screened. Systems that are in a solid phase at $\rho_s = 0$ μM, melt as ρ_s increases. In contrast, increasing the volume fraction favors solidification: The distance between particles decreases and they interact more strongly. As ϕ increases along $\rho_s = 0$, one finds the system changes from a fluid phase into a bcc solid phase and finally into an fcc solid phase.

The values of R, T, and ϵ used in Fig. 1 match those in some of the shear experiments done by Chaikin and coworkers [42–44,51]. The value of Z^* is not directly measurable, but the melting line can be used to determine its value. As shown in Fig. 1, the measured melting point lies above the melting line calculated for $Z^* = 450$ [52]. Good agreement is obtained [52] for the slightly larger value of $Z^* = 625$. While our calculations of sheared systems were all done for $Z^* = 450$, the small difference in effective charge does not appear to alter the dimensionless quantities that we compare to experiment. A

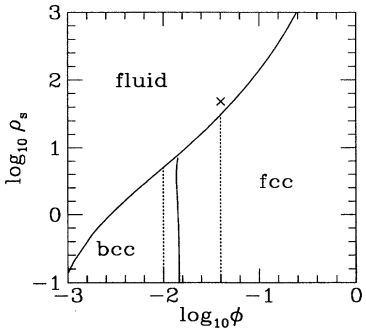

FIG. 1. Calculated equilibrium phase diagram for a colloidal suspension in water at $T = 300$ K with $R = 455$ Å and $Z^* = 450$. The salt concentration ρ_s is in units of μM. Solid lines indicate the melting and fcc-bcc transitions. Dashed lines indicate the volume fractions, 0.01 and 0.04, whose rheology was studied. A cross indicates the experimental melting point at $\phi = 0.04$ for a similar system. This point is consistent with $Z^* = 625$.

much more important factor is the structure of the solid phase. We contrast results for an fcc system ($\phi = 0.04$) and a bcc system ($\phi = 0.01$) in the following sections. The volume fractions corresponding to these systems are indicated by dashed lines in Fig. 1.

B. Time scales

The shear rate, $\dot{\gamma} = \partial v_x/\partial z$, has units of frequency. A dimensionless measure of its magnitude is provided by the Deborah number $\mathrm{De} \equiv \dot{\gamma}\tau$, where τ is a characteristic relaxation time of the system [53]. At low De the system is able to respond to shear and relaxes to a state near equilibrium. For $\mathrm{De} > 1$, the system relaxes more slowly than it is altered by shear. This may produce dramatic changes in the structure of the steady state.

The choice of τ is usually not unique, because most systems have a distribution of relaxation times. The range of time scales is particularly dramatic in solids: Infinite relaxation times are associated with the breaking of translational invariance, and rapid relaxation times are associated with phonon vibrations. We will define De in terms of the rapid vibrational relaxations, keeping in mind that the degree and nature of long-range order may change at arbitrarily small shear rates. In the following, $\mathrm{De} \equiv \dot{\gamma}\tau_E$, where $\tau_E = 2\pi/\omega_E$ is the Einstein period. This is a natural time scale for solids since it describes the oscillations of a single particle with all others held fixed on lattice sites, and because ω_E^2 is the mean of the squares of all phonon frequencies. Other characteristic times are given by a typical interparticle spacing divided by the sound velocity, or by the decay time of the velocity autocorrelation function [54]. All of these are within a factor of two of τ_E. Our simulations cover the range of De from 0.01 to 1.0.

The fluid surrounding colloidal particles produces two major effects that are not incorporated in the simulations described below. One is to change the dynamics from undamped, ballistic motion to overdamped, Brownian motion. While ballistic and diffusional dynamics may in principle lead to different behavior, our studies indicate that only De is relevant. However, the relaxation time in suspensions is quite different from τ_E, because most phonon modes are overdamped [55]. As explained below, the relevant relaxation time is $\tau_{\mathrm{diff}} = a^2/6D$—the time for a free particle to diffuse a typical interparticle distance. The free diffusion constant for spheres is $D = k_BT/6\pi\eta R$, where η is the viscosity of the suspending fluid. For the experimental system of Fig. 1, $D = 4.8\times10^{-8}$ cm^2/s. In the fcc system, $a = 2.15\times10^{-5}$ cm and $\tau_{\mathrm{diff}} = 1.6$ ms. In the bcc system, $a = 3.4\times10^{-5}$ cm and $\tau_{\mathrm{diff}} = 4.0$ ms. Published experiments on the fcc system have gone to $\dot{\gamma} = 300$ Hz or $\mathrm{De} = 0.48$ [42,44].

The surrounding fluid also leads to hydrodynamic forces between colloidal particles. These may become important at high shear rates, but are smaller than the direct Yukawa repulsion for the cases studied here. The restoring force which determines the phonon spectrum and the melting temperature in our simulations is proportional to the energy of a typical phonon mode and thus to the second derivative of the Yukawa potential [36,41]. Dividing the derivative of the hydrodynamic force by the second derivative of the Yukawa potential gives a dimensionless measure of the relative strength of hydrodynamic interactions in determining local structure

$$f = 6\mathrm{De}(\phi^{-1/6} - \phi^{1/6})^{-2}(kT/m\omega_E^2a^2). \tag{2.4}$$

For our parameters, $f < 0.02$ when $\mathrm{De} < 1$. Thus hydrodynamic interactions should be negligible over the range of interest here.

III. SIMULATION METHOD

A. Applying shear

We use a method called the Sllod algorithm [56] (so named because of its close relationship to the Dolls tensor algorithm), which has been extensively used in nonequilibrium molecular dynamics (MD) and shown to agree exactly with adiabatic Couette flow. Our simulation cell is oriented with the shear velocity along the x axis and the velocity gradient along the z axis. Periodic boundary conditions are imposed, and the system is sheared by deforming the cell at a constant rate [57]. The period in each direction, L_i with $i = x, y$, or z, and the total volume, $V = L_xL_yL_z$, are constant.

For reasons discussed below, we have generalized the Sllod algorithm to allow the system to shear along $\hat{\mathbf{y}}$ in response to internal stress using an extension of the Parrinello-Rahman algorithm [57]. An extra equation of motion is added which describes deformations of the periodic cell with displacements along $\hat{\mathbf{y}}$ and gradients along $\hat{\mathbf{z}}$. This degree of freedom is assigned a fictitious mass and responds to a force equal to the internal stress. Previous work suggests that the mass should be roughly 10 times that of the particles, and this is the value used here [58]. We have verified that our results are not sensitive to the mass. Indeed, if the system is large enough, the results do not depend significantly on whether the system can shear along $\hat{\mathbf{y}}$.

Simulations were performed with a fixed number N of spheres, that ranged from 768 to 2592. The equations of motion were integrated using the fifth-order predictor-corrector algorithm [59]. The time step Δt varied between $\tau_E/300$ and $\tau_E/150$, depending on the potential and shear rate. In each case, we checked that the time step was small enough to insure accurate integration. A cutoff radius of $3a$ was used to evaluate the force and potential. This cutoff has been shown to produce negligible changes in the equilibrium properties [36].

B. Thermostats

The energy put into the system by shear must be removed or the temperature will rise. All thermostats proposed to date assume that, locally, the system is close to equilibrium. The temperature is defined in terms of the kinetic energy relative to the mean flow $\mathbf{v}(\mathbf{r}_i)$ at the position $\mathbf{r}_i$ of each particle:

$$3Nk_BT = m\sum_{i=1}^{N}[\dot{\mathbf{r}}_i - \mathbf{v}(\mathbf{r}_i)]^2. \quad (3.1)$$

A constant value of this kinetic temperature can be maintained using any of the methods of equilibrium MD [54]. In our simulations the Nosé-Hoover algorithm [60] was used.

The remaining element needed to define the thermostat is the mean flow $\mathbf{v}(\mathbf{r})$. This is not known *a priori* and may not have the simple linear Couette form expected from Newtonian hydrodynamics: $\mathbf{v}(\mathbf{r}) = \dot{\gamma}z\hat{\mathbf{x}}$. The so-called profile-biased thermostat (PBT) *assumes* Couette flow. Deviations from the linear flow profile are then treated as fluctuations and are damped by the thermostat. To remove this bias, Evans and Morriss introduced a profile-unbiased thermostat (PUT) in which the mean flow is calculated self-consistently [20]. The simulation cell is divided into bins and $\mathbf{v}(\mathbf{r}_i)$ is defined as the average instantaneous velocity of the particles in each bin. Since the components of the mean velocity in each bin are no longer treated as thermal degrees of freedom, the factor N on the left hand side of Eq. (3.1) must be reduced by the number of bins.

As discussed in detail by Loose and Ciccotti [25], there is significant freedom in the choice of bins in the PUT algorithm. One should choose enough bins to allow the system to express any tendency towards nonuniform flow. However, increasing the number of bins decreases the number of modes which are directly coupled to the heat bath. If there are too many bins, thermal fluctuations in $\mathbf{v}$ will not be adequately thermostatted. Recent work by Evans *et al.* [15] used bins containing only 4–11 particles per bin. This only controlled the kinetic energy associated with velocity fluctuations at short wave vectors. Longer wavelength fluctuations were not directly thermostatted and could heat up substantially. We have not explored their thermostat to see how large these effects are. However, we encountered a similar phenomenon when we only controlled the kinetic energy in the $\mathbf{y}$ and $\mathbf{z}$ directions where the mean velocity is expected to vanish. The thermal coupling to fluctuations in the $\mathbf{x}$ direction was slow enough that the effective temperature in this direction more than doubled for simulations with De ≈ 0.1. Evans *et al.* note that their algorithm becomes completely unstable if they further decrease the number of particles per bin. We will return to a discussion of their results in later sections.

The difficulties with defining an appropriate thermostat for De ~ 1 are not surprising. At this shear rate, adjacent lattice planes are moving relative to each other by an interparticle distance in one phonon period, the velocity difference between adjacent planes is about one fifth of the longitudinal sound velocity and twice the rms thermal velocity, and work is being done on the system at a rate of more than kT per particle per τ_E. At such high shear rates the assumption of local equilibrium on which all thermostatting techniques are based becomes questionable. Recent simulations by Liem, Brown, and Clarke [61] show that thermal conduction is not fast enough to remove heat in the center of relatively thin samples ($\sim 50a$) when De exceeds about 0.1. Thus simulations for De ~ 1 are probably not relevant to any atomic system.

The situation is very different in macromolecular systems such as polymers and colloidal suspensions. Long relaxation times associated with large-scale structure determine the Deborah number where shear becomes important. These will be thermostatted by many fast degrees of freedom which remain close to equilibrium. In the case of colloids, the surrounding solvent provides an excellent heat bath whose specific heat is roughly 10^{12} times larger than that associated with changes in ordering of the spheres. The solvent acts much like a PBT thermostat, removing heat homogeneously throughout the system and favoring uniform Couette flow. Measured flow profiles in charge-stabilized colloidal suspensions [2] are consistent with Couette flow.

For these reasons we have performed simulations for De between 0.01 and 1.0 using both the PBT and a version of the PUT. In the latter, we divide the cell into layers that span the system in the x and y plane (cf. Refs. [24] and [25]). In the solid phase, the location and spacing of the layers are usually chosen to correspond to the planes of the equilibrium crystal. As a check, we performed simulations with a larger number of layers (up to four times more) and found no effect on the results. The type of thermostat used for each figure is indicated in the text. Except as noted, the PBT and layered PUT thermostats gave the same results within our accuracy ($\sim 10\%$).

C. Calculating the phase diagram

One method of determining phase boundaries is from the shear rates at which a crystalline state melts or a fluid state crystallizes. However, melting is a first-order phase transition and there may be a large difference between the shear rates where these transitions are observed. The source of this hysteresis is the energy barrier against creation of an interface between the phases. A more accurate melting point can be determined by performing simulations on a system which is constructed with a preexisting interface [14,41,62].

We create an initial configuration in the following manner [14]. A $\dot{\gamma} = 0$ solid phase is formed by placing particles on the sites of a perfect crystal and allowing the system to equilibrate. Particles on the bottom half of the system are then held fixed, while the top half is melted by increasing the salt concentration to a value in the fluid part of the equilibrium phase diagram. When the fluid half has equilibrated, the salt concentration is returned to the initial value and shear is applied. The resulting two-phase configuration has no nucleation barrier preventing growth of either phase, and the more stable one rapidly expands to fill the simulation cell. Note that the initial interface is aligned normal to the velocity gradient so that shear does not force the two phases to mix.

Mechanical equilibrium requires that the shear stress $\sigma \equiv \sigma_{xz}$ in the two phases must be equal. However, the phases may shear at different rates. In fact, experiments show that the total viscosity ($\mu = \sigma/\dot{\gamma}$) of the fluid phase

is greater than that of the solid phases [42]. In order to allow the difference in shear rates to develop, the layered PUT algorithm was used for all two-phase simulations.

The two-phase method has been used previously to calculate the phase diagram of equilibrium [62] and nonequilibrium [14] systems. Recent work on the equilibrium phase diagram of Yukawa systems [41] shows that it is more reliable than the phenomenological criteria used in earlier studies [36,63,64] and that the results agree well with explicit free energy calculations [37].

IV. RESULTS

A. Shear direction and crystal orientation

One important observation from experiments on colloidal crystals is that polycrystalline samples become aligned when shear is applied [1–3,65]. The final orientation maximizes the distances between particles as they shear past each other, and thus minimizes the shear stress [1–3]. The densest lattice planes are stacked along the gradient direction ($\hat{\mathbf{z}}$) to maximize the spacing between successive planes. The nearest-neighbor direction in the planes is parallel to the shear velocity. Lines of particles along this direction are then maximally separated. They lie between similar lines in the planes above and below (see Sec. IV D).

We have studied the effect of crystal orientation in our simulations and find similar behavior. Crystallites which are not in the experimentally observed orientation melt very rapidly—usually before adjacent layers have sheared by a single interparticle spacing. The resulting fluid then recrystallizes with the preferred alignment [66]. In the remainder of this subsection we discuss the favored alignments and shear paths of fcc and bcc crystals. All of the results in following subsections refer specifically to the preferred crystal alignment.

The densest planes in the fcc structure are the close-packed (111) planes and the nearest-neighbor direction in these planes is $\langle 110 \rangle$ (Fig. 2). Successive planes are stacked so that particles are centered over triangular gaps in the plane below. There are three inequivalent plane positions denoted by A, B, and C. In the ideal fcc structure the planes stack in an ABC or ACB sequence.

Figure 2 shows energy contours (solid lines) for an fcc crystal sheared in the close-packed (111) plane. The entire system is sheared coherently without thermal fluctuations and the parameters are those of Fig. 1 with $\phi = 0.04$ and $\rho_s = 0$. Contours are plotted as a function of the relative displacement of a B plane immediately above an A plane (solid circles). As expected, there are large peaks in the energy when particles in adjacent planes are directly above each other. For the case shown, the energy at these maxima is about $6k_BT$ per particle higher than that of the undistorted crystal. If the crystal is sheared in an arbitrary direction it will eventually reach one of these unstable fixed points. Particles can then gain many k_BT by randomly moving away from the peak and it is not surprising that the system melts. Only when the system is sheared along one of the three equivalent nearest-neighbor directions in the (111) plane does the energy remain small.

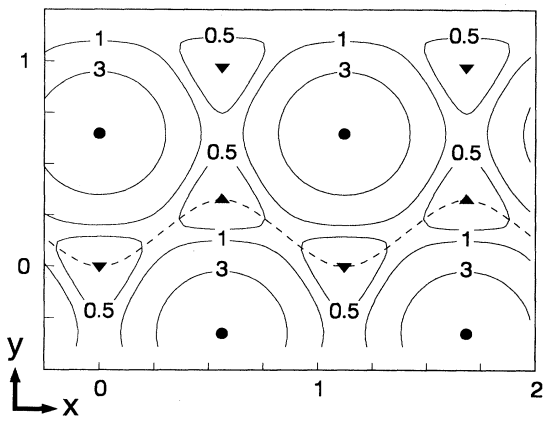

FIG. 2. Energy contours for a fcc crystal sheared coherently in the (111) plane. Circles indicate particle positions in an underlying A plane. Down (up) pointing triangles mark particle positions in undisplaced B (C) planes. The coordinates indicate the displacement (in units of a) of a B plane from its equilibrium position with the underlying A plane held fixed. Contours were calculated for the system of Fig. 1 with $\phi = 0.04$ and $\rho_s = 0$ μM. The energy per particle is normalized by k_BT. The dashed line indicates the minimum energy path given by the condition $\sigma_{yz} = 0$. Arrows indicate the $\hat{\mathbf{x}}$ and $\hat{\mathbf{y}}$ directions. In our simulations, the velocity is along $\hat{\mathbf{x}}$ and the gradient is along $\hat{\mathbf{z}}$.

In our simulations, $\hat{\mathbf{x}}$ coincides with one of these nearest-neighbor directions, and the cell is allowed to deform in the perpendicular direction, $\hat{\mathbf{y}}$, in order to minimize the energy ($\sigma_{yz} = 0$). The minimum energy path is indicated by a dashed line in Fig. 2. While the average direction of the minimum path is along the nearest-neighbor direction, there are pronounced oscillations. The layer hops between the two inequivalent minima at B and C sites. These minima correspond to the two possible fcc twin structures given by ABC and ACB stacking, respectively. By allowing the simulation cell to shear along $\hat{\mathbf{y}}$ we make it possible for the crystal to flow coherently along the minimal path. However, we will show below that the actual motion is not coherent.

The densest planes in a bcc crystal are the (110) planes. They can be viewed as slightly distorted triangular lattices which stack in an ABA sequence. Particles in each plane are centered between four particles in the plane below (Fig. 3). The preferred bcc flow direction is also along the nearest neighbor direction, $\langle 111 \rangle$ in this case. Lines of nearest neighbors along the shear direction are directly centered above similar lines in the plane below. This contrasts with the fcc structure, where the lines are slightly off center, and leads to different structural changes when shear is applied.

Figure 3 shows energy contours (solid lines) for a bcc crystal sheared coherently in the (110) plane. The x and y coordinates correspond to the distances a B plane is sheared relative to an underlying A plane (closed circles)

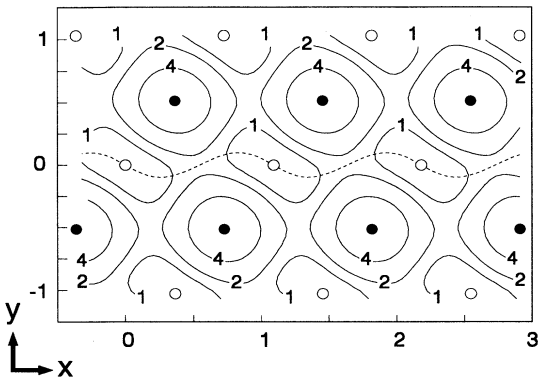

FIG. 3. Energy contours for a bcc crystal sheared coherently in the (110) plane. Closed (open) circles indicate particle positions in A (B) planes. The coordinates show the displacement (in units of a) of a B plane from its equilibrium position with the underlying A plane held fixed. Contours were calculated for the system of Fig. 1 with $\phi = 0.01$ and $\rho_s = 0$ μM. The energy per particle is normalized by k_BT. The dashed line indicates the minimum energy path given by the condition $\sigma_{yz} = 0$. Arrows indicate the $\hat{\mathbf{x}}$ and $\hat{\mathbf{y}}$ directions. In our simulations, the velocity is along $\hat{\mathbf{x}}$ and the gradient is along $\hat{\mathbf{z}}$.

and there are no thermal fluctuations about lattice sites. The parameters are the same as in Fig. 1 with $\phi = 0.01$ and $\rho_s = 0$. As in Fig. 2, energy maxima occur when particles in adjacent planes lie directly above each other and are about $6k_BT$ per particle higher than the equilibrium energy. Crystals sheared in arbitrary directions melt when they pass near these unstable configurations. The minimum energy path (dashed line) lies along one of the equivalent nearest-neighbor directions. Although this path oscillates along $\hat{\mathbf{y}}$, the amplitude of the oscillations is much smaller than in Fig. 2. In addition, there are no inequivalent minima along the shear path, because there are no possible twin structures or stacking faults along the $\langle 110 \rangle$ direction for bcc crystals. This difference between fcc and bcc structures leads to qualitative differences in the sliding mechanism.

B. Nonequilibrium phase diagram

The calculated nonequilibrium phase diagrams for fcc and bcc structures are shown in Figs. 4 and 5. These phase diagrams were calculated using the two-phase method described above, with the solid phase aligned in the preferred shear orientation. Simulations were made for many values of De and ρ_s to determine the stable phase. The figures show only the solid and fluid points closest to the phase boundaries. The system generally contained 768 particles for the fcc simulations, and 864 for bcc simulations. For these values of N the system dimensions were $L_x = 8.98a$, $L_y = 7.78a$, $L_z = 11.00a$ for fcc simulations and $L_x = 8.73a$, $L_y = 9.26a$, $L_z = 10.69a$ for bcc simulations. In both cases, there were 12 layers stacked along the shear gradient. We checked for finite-

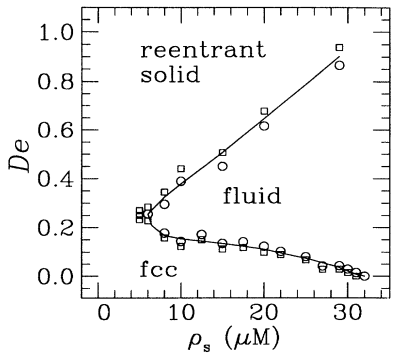

FIG. 4. Nonequilibrium phase diagram for the fcc system of Fig. 1. Calculated bounds on the transition line are indicated by symbols: squares for the solid phase and circles for the fluid phase. The solid line is a guide to the eye.

size effects by increasing N by a factor of 4 and doubling both L_x and L_z. The only change was that a narrow coexistence region appeared about the phase boundaries in Figs. 4 and 5. Within this region, neither phase expanded to fill the entire system during the course of our longest runs. A coexistence region is expected at a first order melting transition, but since its width was comparable to the uncertainties in our plotted phase boundaries ($\sim 5\%$) we did not explore it further.

The fcc and bcc phase diagrams in Figs. 4 and 5 are clearly similar. However, it is difficult to compare them directly because ρ_s has different effects at the two values of ϕ. A dimensionless measure of the effective temperature is provided by the ratio of T to $T_m^{\rm eq}$, the equilibrium melting temperature for the potential (specified by U_0 and κ in Eq. 2.1) [67]. As seen in Fig. 6, the fcc and bcc phase boundaries show an amazing commonality when plotted in terms of De and $T/T_m^{\rm eq}$. This suggests that the phase transitions for the two solid structures share common origins and mechanisms.

For both structures, the shear-melting transition temperature T_m decreases smoothly from $T_m^{\rm eq}$ as De increases

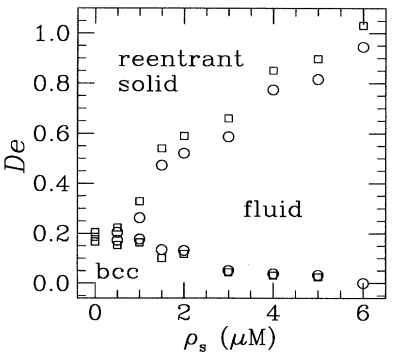

FIG. 5. Nonequilibrium phase diagram for the bcc system of Fig. 1. Calculated bounds on the transition line are indicated by symbols: squares for the solid phase and circles for the fluid phase.

from zero. This indicates that the shear-melting transition evolves continuously from the equilibrium transition. An increase in shear rate acts like an increase in the effective temperature. Particles are forced past each other more rapidly, and have less time to establish positional correlations. Since correlations are responsible for lowering the energy of the solid phase relative to that of the fluid, the region of solid stability decreases.

Density functional calculations [8,9] have started from the assumption that shear melting could be described as a perturbation from equilibrium melting, and predicted that the value of ρ_s or $T/T_m^{\rm eq}$ at melting should decrease as De^2. While our results are consistent with a perturbative approach, the analytic behavior is markedly different. The values of $T/T_m^{\rm eq}$ and ρ_s at melting decrease roughly linearly as De increases from zero. A linear decrease is also found in the experimental data shown in Fig. 6 and discussed further below [42,44]. The origin of this discrepancy between density functional results and simulation and experiment is explained in Sec. IV C.

As De increases above about 0.2, the phase boundary between solid and fluid phases makes a dramatic turn. At low ρ_s, where $T/T_m^{\rm eq} \lesssim 0.5$, there is no shear-melting transition. At higher ρ_s there is a reentrant transition to a solid phase at large De. In the reentrant regime, shear induces *order*. For $\mathrm{De} \sim 1$, shear dominates the temperature in determining the structure. As will be shown in the next subsection, order reduces the shear stresses by decreasing the frequency of collisions. The weaker equilibrium solids (higher $T/T_m^{\rm eq}$) require larger De to enforce an ordered structure. At sufficiently high De, even systems with an equilibrium fluid phase can be solidified.

The origin of the reentrant phase can be understood in terms of an attractive interaction which is loosely analogous to that which produces superconductivity. When a particle is sheared along a path, it pushes other particles out of the way and creates an empty region in its wake. Nearby particles will feel an attraction to this cleared path, and will tend to align into strings of particles parallel to the shear velocity. Strings with the same

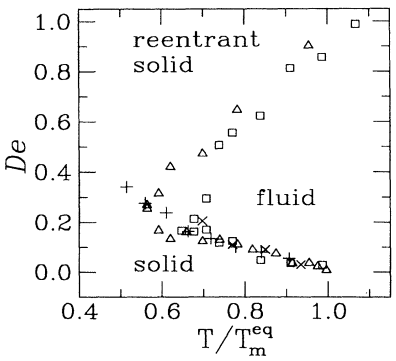

FIG. 6. Normalized phase boundaries calculated for the fcc (△) and bcc (□) systems of Fig. 1. Plotted points are midway between the bounds on the transition lines shown in Figs. 4 and 5. Normalized experimental results for the melting transition of fcc systems at $\phi = 0.04$ (×) and 0.05 (+) are also indicated [44].

z coordinate are not sheared past each other and will have time to establish long range two-dimensional order. Successive planes cannot become correlated along $\hat{\mathbf{x}}$, but lines of atoms parallel to $\hat{\mathbf{x}}$ can become registered in the $\hat{\mathbf{y}}$ direction. As shown in later subsections, this is the structure which we observe in the reentrant regime.

Experimental results obtained by Chaikin *et al.* [42,44] for the fcc system can be compared directly to the scaled theoretical results shown in Fig. 6. Equilibrium melting is observed at $\rho_s \approx 50\ \mu M$ which is consistent with $Z^* = 625$ [41]. Values of $T_m^{\rm eq}$ at other ρ_s are computed from the equilibrium phase diagram [41] without any additional unknown parameters. The value of $\dot{\gamma}$ at melting is determined from the stress discontinuity in experimental stress vs strain-rate curves (see next subsection). Multiplying by the relaxation time, $\tau_{\rm diff} = 1.6$ ms (1.4 ms) for $\phi = 0.04$ (0.05), one obtains De. Experimental points normalized in this way are shown as crosses (plusses) in Fig. 6, and lie remarkably close to the theoretical curves. This supports the notion that ballistic and Brownian systems have closely related nonequilibrium phase diagrams. Although the relaxation times in De are only defined up to a constant of order unity, the definitions used here are independently confirmed by comparisons of calculated and measured stresses in the fluid phase (Sec. IV C).

Note that Chaikin *et al.* [42,44] did not observe shear-melting for $T/T_m^{\rm eq} < 0.5$. This corresponds closely to the lowest $T/T_m^{\rm eq}$ where melting is observed in our calculations. However, their experimental apparatus had a limited operating range that prevented exploration of higher De at low salt concentrations. Results for the fcc system at $\rho_s \leq 30\ \mu M$ and $\phi = 0.04$ only extended to $\mathrm{De} = 0.32$. While this indicates an upturn in the phase boundary, it does not conclusively support the absence of melting at low $T/T_m^{\rm eq}$. More conclusive evidence comes from recent experiments by Evans *et al.* [15]. They studied suspensions with the same sphere diameter and nearly the same concentration $\phi = 0.0439$, but in a different solvent. The equilibrium structure was bcc rather than fcc and the salt concentration at melting was different. Evans *et al.* found that a suspension with $\rho_s = 0$ remained solid for $\dot{\gamma}$ as high as 2×10^4 Hz ($\mathrm{De} \sim 30$). In contrast, systems with $\rho_s = 25\ \mu M$ melted at $\dot{\gamma} = 43$ Hz ($\mathrm{De} \sim 0.07$). Thus there is good experimental evidence that colloidal solids which are well below their equilibrium melting temperatures do not shear melt.

Evidence from simulations and experiments for a reentrant solid phase at high De is much less conclusive. Shear-induced order has been observed in several experiments at volume fractions near the freezing point for hard spheres [12,23]. Chaikin *et al.* did not go to high enough shear rates to observe the reentrant phase in their more dilute systems [42,44], but Evans *et al.* found that their $\rho_s = 25\ \mu M$ system did not recrystallize for $\dot{\gamma}$ as high as 3890 Hz ($\mathrm{De} \sim 6$). This system appears to be relatively far from the transition between systems which shear-melt and those that do not (e.g., 0 μM). Based on the value of $\mathrm{De} \approx 0.07$ at melting, we would predict a reentrant transition near $\mathrm{De} = 0.6$. It is possible that hydrodynamic interactions become important by this point and modify

the phase diagram. Experimental studies near the lowest value of ρ_s where shear melting is seen might reveal a reentrant phase at lower De where hydrodynamic effects would be smaller. It is clear that the melting line must exhibit interesting behavior in this region—either rising precipitously or becoming reentrant.

Simulation studies have also reached conflicting conclusions about the presence of reentrant solid structure. The results seem to depend predominantly on which of the thermostats described in Sec. III B is used, rather than on the potential, system size, or other parameters. Reentrant phases have been found by a number of groups using the PBT or the layered PUT [11,14,22,24,25]. Our results [14] and those of Evans *et al.* [15] show that these two thermostats yield nearly equivalent phase boundaries (within $\sim 10\%$). The reentrant phase is only suppressed in simulations where fewer degrees of freedom are thermostatted [15,20]. Our belief is that these simulations allow heating at long wavelengths and that this destroys the reentrant phase. Colloidal suspensions are well thermostatted by the surrounding solvent at all length scales and we suspect that any deviations between experiment and results of PBT or layered PUT simulations reflects other effects of the solvent, including hydrodynamic interactions and turbulence.

C. Stress vs shear rate

The variation of shear stress with strain rate provides another quantitative test of our simulations. Chaikin *et al.* [42,44] found that their experimental data collapsed onto universal solid and fluid curves when the stress was normalized by the measured polycrystalline shear modulus G and plotted against $\dot{\gamma}$. This collapse is shown in Fig. 7. While the data for the equilibrium fluid case ($\rho_s = 50\ \mu M$) lies slightly below the other fluid curves, this is probably because G could not be measured and a calculated value was used [44]. To facilitate comparison with our simulations, $\mathrm{De} = \dot{\gamma}\tau_{\mathrm{diff}}$ is indicated on the top axis of Fig. 7 and σ/c_{44} is plotted on the right axis [68].

Results from our simulations for the fcc and bcc systems are shown in Figs. 8 and 9, respectively. Both the shear stress and the normal stress, $N_1 \equiv \sigma_{zz} - \sigma_{xx}$, collapse onto universal solid and fluid curves when normalized by c_{44} and plotted against De. The value of τ_E changes substantially with ρ_s and the curves do not collapse when plotted against $\dot{\gamma}$. Hence the success of the collapse of experimental curves in Fig. 7 indicates that the relevant relaxation time in experiments is independent of ρ_s. The diffusion time τ_{diff} meets this criterion, but any time related to interparticle interactions does not. This justifies our use of τ_{diff} in Fig. 6 and in the top axis of Fig. 7.

The dotted line in Figs. 7–9 shows calculated values of σ/c_{44} for the fluid phase at the equilibrium melting point of the fcc system ($\rho_s = 31\ \mu M$). This line agrees quite well with the experimental curve taken just above the melting point ($\rho_s = 50\ \mu M$) in Fig. 7. Both curves also show pronounced non-Newtonian behavior: The differential viscosity, $d\sigma/d\dot{\gamma}$, drops by more than a factor of 2. Non-Newtonian behavior is also evident from the large calculated normal stress in Fig. 8(b). The value of N_1 rises to about 10% of the shear stress. Although the interparticle potential for the bcc system is quite different, the calculated fluid response is nearly identical to that for the fcc system. Similar response curves have also been obtained in studies of simpler interparticle potentials [69].

The universal curves for the solid phases show a finite yield stress $\sigma^{(y)}$ in the limit $\mathrm{De} \to 0$. Linear fits to the calculated curves give $\sigma^{(y)} = 0.016 c_{44}$ for the fcc system and $\sigma^{(y)} = 0.006 c_{44}$ for the bcc system. The former value agrees well with the apparent experimental yield stress of $\sigma^{(y)} \approx 0.02 c_{44}$ for fcc systems. However, experiments

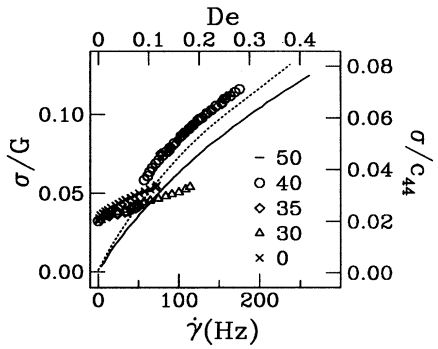

FIG. 7. Normalized shear-rate vs shear-stress curves for the indicated ρ_s (in μM) from Ref. [44]. The stress is normalized by the polycrystalline modulus G on the left axis and by c_{44} on the right axis. The bottom axis indicates $\dot{\gamma}$ and the top shows $\mathrm{De} = \dot{\gamma}\tau_{\mathrm{diff}}$. A dotted line shows the calculated stress from Fig. 8 for the equilibrium fluid state at $\phi = 0.04$, $\rho_s = 31\ \mu M$.

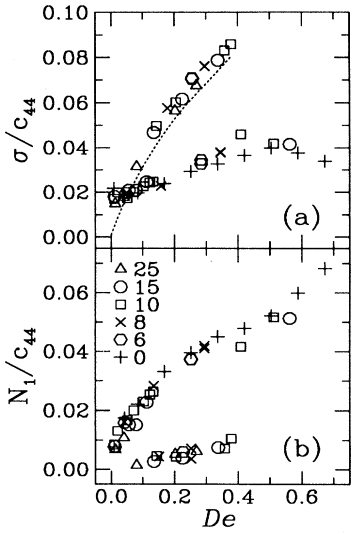

FIG. 8. Calculated variation with De in (a) shear stress and (b) normal stress for the fcc system at the indicated values of ρ_s (in μM). The dotted line shows the shear stress for the equilibrium fluid state at $\rho_s = 31\ \mu M$.

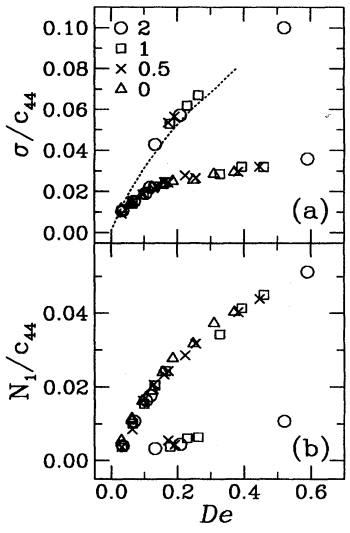

FIG. 9. Calculated variation with De in (a) shear stress and (b) normal stress for the bcc system at the indicated values of ρ_s (in μM). A dotted line shows the shear stress from Fig. 8 for the equilibrium fluid state at $\phi = 0.04$, $\rho_s = 31\ \mu M$.

at very low shear rates show that there is no true yield stress. The value of σ begins to decrease towards zero for $\dot{\gamma} < 0.1$ Hz (De $< 10^{-4}$). This change in experimental behavior suggests a change in the mechanism of shear flow. Unfortunately, simulations in this regime are not currently feasible.

As De increases from zero, the calculated and measured shear stresses in the solid phases rise gradually from $\sigma^{(y)}$. The calculated normal stresses rise rapidly from zero at De $= 0$, and exceed σ for De $\gtrsim 0.1$. Preliminary experimental measurements on the solid fcc phase also show that N_1 exceeds σ [70].

When the melting point is reached, the shear and normal stresses jump discontinuously to the fluid curves. The increase in σ as the solid melts may seem surprising, since one expects a fluid phase to flow more readily than a solid. However, the solid phase is oriented to minimize σ by maximizing the separation between particles as they shear past each other. The fluid phase is disordered, and at high shear rates particles do not have time to avoid each other. Hence shear produces more interparticle collisions in the fluid phase, and the stress exceeds that in an aligned solid for De greater than about 0.05. Note that the calculated stress for other solid orientations is higher than that in the fluid phase, but that these orientations melt at the lowest De studied here.

A second discontinuity in the calculated values of σ and N_1 occurs at higher De. This discontinuity marks the shear-induced ordering transition to the reentrant solid phase, and σ and N_1 switch back to the universal solid curves. Experiments on hard sphere systems also show a shear-thinning transition to a reentrant solid phase [12].

Solid bcc and fcc phases have quite different shear stresses. In the bcc phase, σ rises relatively rapidly until De ≈ 0.1 and then levels off at about $0.025c_{44}$. Higher stresses and an interesting flow instability are observed in the fcc phase. We find that σ reaches a maximum value of about $0.045c_{44}$ and then begins to decrease with increasing De, *if the* PBT *is used.* This is one of the few cases where the PBT and PUT algorithms produce qualitatively different results.

When $d\sigma/d\text{De} < 0$ (De > 0.4), uniform shear is linearly unstable. Layers that slip more rapidly feel less stress and accelerate, while slower layers are decelerated. The PBT algorithm suppresses this instability and allows us to obtain σ vs De in the unstable region. If the PUT thermostat is used, the system lowers σ by localizing all the strain at a few planes. The regions between these planes move together as rigid blocks. The transition to nonuniform shear is illustrated in Fig. 10 which shows PUT velocity profiles for De $= 0.3$ and 0.5. Both profiles were averaged over $5000\Delta t$. The profile for De $= 0.3$ is within thermal fluctuations of the linear profile corresponding to uniform Couette flow (dotted line). In contrast, the profile for De $= 0.5$ shows that the system has broken into three comoving blocks. All of the strain is localized at their interfaces which lie at $z/L_z = 0.3$, 0.5, and 0.95. It is not clear whether this flow instability will also occur in colloidal systems, because the surrounding solvent favors Couette flow. This may change the onset of the instability or suppress it completely, as in the PBT simulations.

The calculated stress curves give important insight into the shape of the nonequilibrium phase diagram. The density functional theories mentioned above assumed that the thermodynamic and correlation functions of sheared systems could be expressed in terms of a power law expansion about equilibrium properties [8,9]. They then argued that the lowest order contribution from shear scaled as De^2, since reversing the direction of shear does not alter the system. However, the product σDe also has the correct symmetry. Moreover, this product has an appealing physical interpretation. One expects that the increase in free energy due to shear is related to the deviation from equilibrium imposed by energy dissipation. The rate of energy dissipation per unit volume times the relaxation time is precisely σDe.

For the fluid, $\sigma \propto$ De and the leading changes from equilibrium are indeed of order De^2. In a solid with a yield stress, the leading terms are of order $|\text{De}|\sigma^{(y)}$. Thus, to lowest order in De, the difference between sheared solid

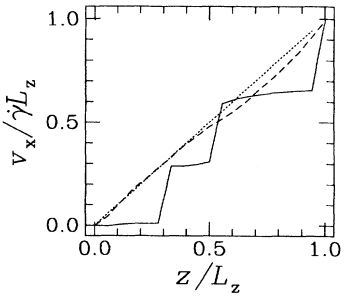

FIG. 10. Flow profiles for the fcc system at $\rho_s = 1\ \mu M$. Uniform Couette flow is indicated by the straight dotted line. Dashed and solid lines show the observed profiles for De $= 0.3$ and 0.5, respectively. L_z is the height of the simulation cell.

and fluid free energies is:

$$F_s(\mathrm{De}) - F_l(\mathrm{De}) \approx F_s(0) - F_l(0) + K\sigma^{(y)}\mathrm{De} \quad (4.1)$$

$$\approx \Delta L(T - T_m^{\mathrm{eq}})/T_m^{\mathrm{eq}} + K\sigma^{(y)}\mathrm{De}, \quad (4.2)$$

where ΔL is the latent heat per unit volume and K is a dimensionless constant. An estimate of K can be obtained from the increase in energy of the solid phase with De. For the fcc phase we find $K \sim \Delta E_s/\sigma^{(y)}\mathrm{De} \approx 3$.

The nonequilibrium melting temperature is given by setting Eq. (4.2) to zero:

$$T/T_m^{\mathrm{eq}} - 1 = -K\sigma^{(y)}\mathrm{De}/\Delta L. \quad (4.3)$$

The predicted melting temperature decreases linearly with De as found in Fig. 6. The initial slope, $-K\sigma^{(y)}/\Delta L$, can be obtained from the yield stresses quoted above and values of ΔL reported in Ref. [36]. We find $-0.5K$ for the fcc system and the observed slope on Fig. 6 is about -2. These values are in reasonable agreement, given our estimate of K. Our assumptions work less well for the bcc system since σ is roughly twice $\sigma^{(y)}$ at the first data point on the phase diagram. However, the results remain roughly consistent with our crude arguments for the transition point.

D. Structure

Figures 11 and 12 show projections of instantaneous particle positions onto the yz plane for fcc and bcc solids,

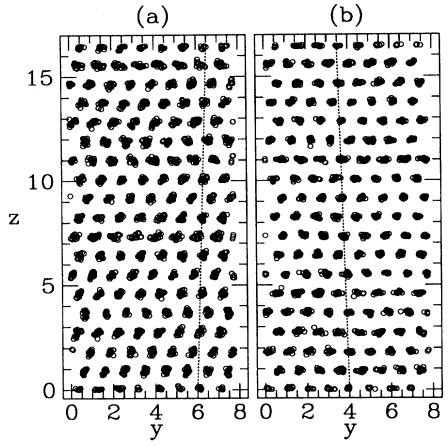

FIG. 11. Projections of sheared fcc solids onto the yz plane at (a) De = 0.05 and (b) De = 0.8. Note that particles lie on well-defined layers normal to the z direction and on lines parallel to x within each layer. At low De, the successive layers tend to lock in one of the preferred close-packed stacking positions. However, the original ABC stacking sequence becomes interrupted by stacking faults whose number increases with De and time. Dashed lines in each panel indicate the y coordinate of particles in A planes. The sequence in panel (a) corresponds to $ABCABACACABACBCABCA\ldots$. As De increases, the stacking sequence gradually changes to a regular alternation between A and B'. The A, B, C, and B' configurations are illustrated in Fig. 14.

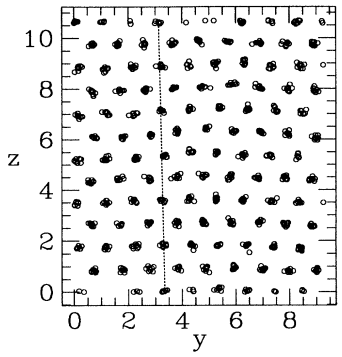

FIG. 12. Projections of a sheared bcc solid onto the yz plane at De = 0.06. Particles form sharp layers and lie on lines parallel to $\hat{x}$ within each layer. As in unsheared crystals, the layers stack in an alternating AB sequence. A dashed line indicates the y coordinate of particles in A layers.

respectively. In each case, particles lie on well-defined layers normal to $\hat{\mathbf{z}}$. The rms displacement of particles in the z direction is much smaller than the interlayer spacing. The ratio reaches values expected from a Lindemann criterion as the melting transition is approached.

These yz projections also show that particles within each layer order into lines along $\hat{\mathbf{x}}$. Each line collapses onto a small area in the yz plane. The spread of the projected positions is anisotropic. Although the degree of anisotropy varies with De, the rms particle displacement in the y direction is consistently larger than that in the z direction.

The structure within selected fcc and bcc layers is shown in Fig. 13. Note that they retain much of the structure of the corresponding unsheared solids. However, there are systematic changes in the degree and type of disorder. Fcc and bcc systems exhibit somewhat different behavior and we will discuss them separately.

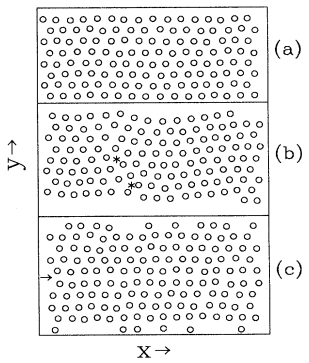

FIG. 13. Structure of layers normal to $\hat{\mathbf{z}}$ for $\rho_s = 0$ μM. Panel (a) shows enhanced fluctuations about lattice sites at De = 0.04 in a fcc crystal. At De = 0.25 (b) in-plane dislocations (marked by $*$) are found. Panel (c) shows the structure of a bcc layer in a crystal sheared at De = 0.03. An arrow indicates the location of a twin boundary in the sheared system. The lines of atoms on either side of the boundary are directly above each other.

In an unsheared fcc crystal, particles in each layer vibrate about the sites of ideal hexagonal close-packed lattices. As De rises from zero, the degree of disorder increases. This loss of order can be understood in several ways. One is that shear brings the crystal through higher energy configurations where the restoring forces on particles and the energy barriers for diffusion are smaller. A second is that shear brings particles past more sites in the adjoining planes, thereby increasing the likelihood of strong collisions.

At low shear rates, the lattice structure of the planes remains intact [Fig. 13(a)]. However, the amplitude of oscillations about lattice sites increases with De. At somewhat larger shear rates, a few particles diffuse between layers producing vacancy-interstitial pairs. The concentration of these point defects rises with De, reaching up to 2% at the melting transition. This is much larger than the density of point defects seen at the melting transition in our equilibrium simulations ($< 0.2\%$).

Vacancies and interstitials do not disturb the long-range order within layers or the registry between adjacent layers. More profound deformations of the layers are observed close to the melting transition. Figure 13(b) shows a pair of dislocations which formed within an *individual* layer. They decrease the alignment of particles along the shear direction, and reduce the registry with neighboring layers. In particular, lines of atoms along x are no longer channeled smoothly between corresponding lines in the planes below. This misorientation of lines appears to be particularly destabilizing, and is only seen close to the melting transition.

Within the reentrant regime, the degree of disorder *decreases* with increasing De. In systems which melt, the disorder begins to decrease above the refreezing transition. In systems which do not melt ($\rho_s < 6\ \mu M$ for $\phi = 0.04$), disorder decreases for De > 0.25. By De ~ 0.7 most of the defects that formed at intermediate shear rates have been annihilated. The remaining degree of disorder is similar to that shown in Fig. 13(a).

Similar structural changes are seen in the layers of shearing bcc systems. The major difference is that the bcc layers exhibit an additional type of deformation—in-plane twin boundaries. In an unsheared bcc crystal, particles vibrate about the sites of a distorted triangular lattice (Fig. 3). The two possible orientations of the distortion correspond to two twin structures which are related through a reflection in the xz plane. As shown in Fig. 13(c), shear produces twin boundaries within individual bcc layers. These twin boundaries appear at the lowest studied shear rates. They do not penetrate the entire system and are not stationary. Indeed, their motion appears to be an important feature of the shear mechanism in bcc solids.

E. Shear-flow mechanism

Simulations can determine the mechanism of shear flow directly by following the motion of individual particles. Possible flow mechanisms include layer-over-layer sliding, sliding at grain boundaries, vacancy motion, and dislocation motion. The close correspondence between experimental and theoretical stress curves indicates that our simulations correctly reproduce the major shear mechanism. We find that layer-over-layer sliding dominates for $0.01 <$ De < 1. This is not surprising, given that the crystal orientation observed in both theory and experiment [2,3] minimizes the stress for interlayer sliding. The observed densities and velocities of vacancies, interstitials and dislocations are too small for them to play an important role. Grain boundary sliding is only important in specific limits. For example, the co-moving blocks found in the fcc system for De > 0.4 may be viewed as platelike grains which slide over each other. A more dramatic example of grain boundary sliding has been observed [4] in experiments at De $< 5 \times 10^{-4}$. The sample breaks up into spherical grains that rotate like ball-bearings between the walls of the experimental cell. This large length-scale, low De behavior is far beyond the range of our studies.

In fcc crystals, the diffusion of particles relative to others in the same layer is much less than a lattice constant on the time span of our simulations. Thus the entire layer moves coherently and its position can be described by a single coordinate—the average particle displacement. At low De, one expects [2,3] that the relative motion of adjacent close-packed planes will follow the minimum energy path shown in Fig. 2 and reproduced at the top of Fig. 14. To test this conjecture, we calculated the differential displacement between two planes, $\Delta\mathbf{r}$, as a function of time. As shown in Fig. 14, $\Delta\mathbf{r}$ follows the zig-zag minimum path quite closely at De $= 0.02$. However, the motion is not uniform. Instead, $\Delta\mathbf{r}$ sticks for prolonged intervals at positions corresponding to the low energy B and C stacking positions.

The intermittent nature of a plane's motion is more clearly seen in Fig. 15 which shows the time dependence of the x and y components of $\Delta\mathbf{r}$ for De $= 0.02$. Note the pronounced plateaus where the planes have locked into a favorable stacking sequence. These are separated

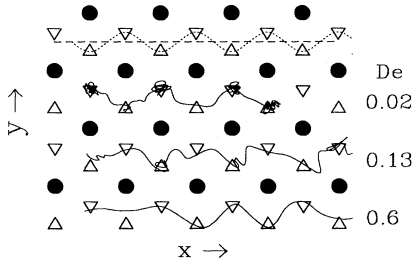

FIG. 14. Trajectories of the interlayer displacement, $\Delta\mathbf{r}$, of an fcc plane over an A layer (•). Local energy minima occur at the B (△) and C (▽) positions. The dotted line at the top shows the minimum energy path for $T = 0$. The straight dashed line is the trajectory for which $\sigma_{xz} = 0$. We call this plane position B'. Solid lines show typical trajectories for $\rho_s = 10\ \mu M$ at De $= 0.02$, De $= 0.13$ (just below melting), and De $= 0.6$ (reentrant phase), in order of decreasing height. The displacement locks for varying intervals at B and C positions. In this figure, locking produces wiggles about the local energy minima.

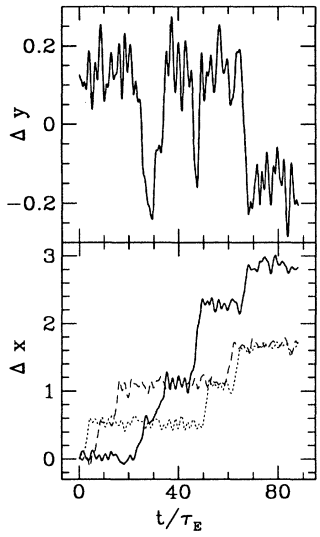

FIG. 15. Solid lines illustrate the intermittent motion along one of the fcc trajectories in the preceding figure: $\rho_s = 10\ \mu M$ at De = 0.02. Both x and y components of $\Delta\mathbf{r}$ are plotted against time t. The upper layer advances along $\hat{x}$ in a sequence of sudden jumps. The time interval between jumps varies widely, and the layer spends the majority of the time locked in a favorable B ($\Delta y < 0$) or C ($\Delta y > 0$) stacking position. Broken lines show Δx for two other pairs of neighboring planes in the same system. Note that they also advance in a sequence of sudden jumps, but at different times. The change in Δx during a jump is always quantized and corresponds to the distance between favorable stacking configurations.

by sudden jumps where the upper plane slides forward to a new local energy minimum at a B or C position. The length of the plateaus between jumps is not uniform, and different planes in the system jump forward at different times. This creates stacking faults which are clearly evident in Fig. 11(a). These appear at the lowest studied shear rates and increase in number with De and the length of the simulation. The final state seems to be a nearly random stacking sequence of close-packed planes. This explains why allowing the simulation cell to shear in the y direction does not produce significant changes in the results. The cell geometry would only play an important role if layers moved coherently on length scales comparable to L_z.

As De increases, the relative displacement is less able to follow the minimum path (Fig. 14). There is also less locking at favorable stacking positions. The plateaus seen in Fig. 15 completely disappear by De = 0.6. A corresponding change occurs in the stacking of layers. As shown in Fig. 12(b), the layers alternate between A and B' configurations, where B' is halfway between B and C positions (Fig. 14). At these De, layers shear so rapidly that adjacent layers do not have time to shift laterally. They settle into an AB' sequence which represents the best time-averaged alignment [3].

Trajectories of adjacent planes in shearing bcc crystals are shown in Fig. 16. Even at low De, planes do

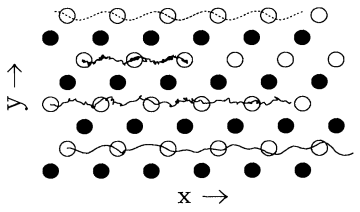

FIG. 16. Trajectories of the interlayer displacement, $\Delta\mathbf{r}$, of a bcc plane over an A layer (•). Local energy minima occur at the B (○) sites. The dotted line at the top shows the minimum energy path for $T = 0$. Solid lines show typical trajectories for $\rho_s = 0\ \mu M$ at De = 0.01, De = 0.06, and De = 0.38 (reentrant phase), in order of decreasing height.

not move coherently along the minimal path. Although the trajectories have oscillations along y whose amplitude is comparable to those on the minimal path, the oscillations do not have a well-defined period or amplitude. Figure 17 shows the time dependence of $\Delta\mathbf{r}$ for De = 0.01. The relative displacement between neighboring planes increases in a series of steps, but the transitions between plateaus are much more gradual than in the fcc system. The height of the steps is not well quantized, and is often much less (0.3–0.5a) than the distance between local minima on the minimal path (1.1a). In addition, the shear rate at which the steps disappear (De < 0.06) is more than an order of magnitude smaller than in the fcc system. All of these differences indicate that the bcc

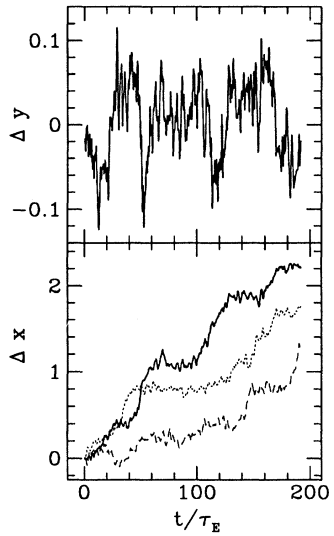

FIG. 17. Solid lines illustrate the intermittent motion along one of the bcc trajectories in the preceding figure: $\rho_s = 0\ \mu M$ at De = 0.01. Both x and y components of $\Delta\mathbf{r}$ are plotted against time. Broken lines show Δx for two other pairs of neighboring planes in the same system. The plateaus in Δx are more rounded than in the fcc system, and the transitions between them are more gradual. The forward advance between plateaus is not well quantized and is typically smaller than the distance between local energy minima in the preceding figure.

planes move less coherently than fcc planes. Our structural studies indicate that the formation and motion of twin boundaries is responsible for this loss of coherence. More detailed studies of the microscopic shear mechanism are currently underway [71]. They reveal that particles within a line along the $\hat{\mathbf{x}}$ direction move together, but that lines within the same plane advance at slightly different rates due to twin boundary motion [71].

Many of the above conclusions about the shear mechanism can also be deduced from the time-averaged stress curves discussed in Sec. IV C and the rms fluctuation in the stress, $\delta\sigma$. The stress along the minimal paths oscillates between $-\sigma_{\max}$ and $+\sigma_{\max}$, where $\sigma_{\max}/c_{44}$ is about 0.045 for the fcc system and 0.09 for the bcc system. The average value of σ is identically zero, since there is no net energy change. Thus the time-averaged stress would vanish if the planes sheared over each other at constant velocity. The observation of a yield stress indicates that the planes move nonuniformly, slowing (accelerating) when the stress opposes (favors) their advance. In the fcc case, the layers actually stick at local energy minima and the yield stress is nearly half of $\sigma_{\max}$. Bcc layers slide more uniformly. As a consequence, the yield stress is much smaller than $\sigma_{\max}$, and σ varies more rapidly with De than in the fcc system.

If all planes slowed and accelerated in phase, the total stress in the system would still oscillate between $\pm\sigma_{\max}$. In contrast, we find that fluctuations in the stress are smaller than the mean value ($\delta\sigma < \sigma < \sigma_{\max}$) [72]. This is consistent with the observation that planes move incoherently. The small size of $\delta\sigma$ also implies that the difference between constant stress and constant strain rate simulations is not great at the system sizes considered here.

Ackerson and co-workers have studied the structure factor of sheared fcc and bcc systems [2,3]. They also concluded that the dominant shear mechanism was layer-over-layer sliding. Their results for fcc systems show a transition from random stacking of close-packed layers to an AB' stacking as De increases [3]. Scattering from sheared bcc crystals shows a superposition of the two twin structures [2]. These results are consistent with our simulations, and a detailed comparison to scattering measurements will be presented in a future paper [71].

To interpret their results, Ackerson *et al.* [2] developed a simple zero-temperature model in which planes moved coherently along minimal energy paths. The inertia of the planes made them less able to follow zig-zags in the minimal paths as De increased. Some aspects of this model are consistent with the trajectories described above. However, there are two important differences. The first is that the motion of fcc planes is far less coherent than the model would predict. Planes lock together for a period and then jump to a new configuration. There are pronounced deviations from the minimal path due to thermal fluctuations.

The second difference is that Ackerson *et al.* [2] also allowed each layer to shear coherently within the xy plane to maintain $\sigma_{xy} = 0$. This reduces the maximum stress needed to shear the solid. The effect is most dramatic for bcc solids where they predicted that the entire lattice would deform coherently from one twin to the other. To check their conclusions, we performed a separate set of bcc simulations which allowed deformations in the xy plane in addition to shear within the yz plane (see Sec. III A). However, adding this extra degree of freedom did not produce significant changes in any of our bcc results. Apparently, the simulation cells are too large to shear coherently at the studied shear rates. Instead, twin boundaries appear within individual bcc layers [71].

V. CONCLUSIONS

We have presented detailed studies of the phase diagram, stress, structure and flow mechanism for sheared systems. The results are in good quantitative agreement with previous experiments on charge-stabilized colloidal suspensions [42–44]. Several predictions are made which we hope will be tested by future experiments.

A dimensionless nonequilibrium phase diagram was constructed by scaling the temperature by the equilibrium melting temperature and multiplying the shear rate by a characteristic relaxation time (Fig. 6). Experimental results for fcc systems and theoretical results for fcc and bcc systems fall onto nearly universal transition lines on this phase diagram. Shear plays a dual role, destabilizing the equilibrium crystal at low shear rates and stabilizing an ordered phase at high shear rates.

The melting transition temperature decreases linearly from $T_m^{\rm eq}$ as De increases from zero. Although there is no general criterion for the onset of nonequilibrium phase transitions, this region of the phase diagram can be understood by assuming that a shear-rate dependent "free energy" functional is minimized. Previous theories had assumed that the lowest order deviations from equilibrium quantities [8,9] scaled as De^2. The presence of a finite yield stress in the solid phase (Figs. 7–9) leads to terms of order $|\sigma^{(y)}\mathrm{De}|$. This is a natural measure of the shift in the effective free energy since it corresponds to the energy dissipated in a characteristic relaxation time. The slope of the transition line is consistent with the rate of increase in the internal energy of sheared solids.

As De approaches 0.25, the melting line begins to turn around. Solids with $T/T_m^{\rm eq} \lesssim 0.5$ never melt. Solids with $T/T_m^{\rm eq} \geq 0.5$ first melt and then reorder at high De. There is clear experimental evidence that the melting line turns upwards as De increases and that low temperature solids do not melt [15,44]. It is less clear whether there is a reentrant solid phase at higher temperatures. Some groups have seen reentrant order [12,23] while others [15] have not. One possible explanation is that hydrodynamic interactions suppress the reentrant phase. The magnitude of these interactions is different in each experiment. Hydrodynamic effects can be minimized in future experiments by using small volume fractions and low shear rates. Experiments near the upturn in the melting line have the greatest chance of observing the reentrant phase. It will also be important to test the effect of hydrodynamic interactions and Brownian dynamics on calculated phase diagrams.

The shear and normal stress also collapse onto universal fcc, bcc, and fluid curves when normalized by c_{44} and plotted against De. Calculated and measured values of the fcc and fluid shear stresses are in excellent agreement. There are no reported measurements of the shear stress in the bcc phase or of the normal stress in any of the three phases. Such measurements would provide a further quantitative check of our simulations.

The calculated shear stresses in fcc and bcc phases are quite different. The dimensionless yield stress is almost three times smaller in the bcc phase, even though the maximum stress on the minimal path is larger. This discrepancy results from differences between the shear mechanisms for the two phases. When fcc systems are sheared slowly, layers slide over each other in an erratic sequence of hops between local energy minima. The mean stress is high because layers spend little time in low stress configurations between hops. In bcc systems, layers slide through the generation and motion of in-plane twin boundaries. This lowers the maximum stress required to initiate motion of layers. The mean stress is further lowered because bcc planes slide over each other more smoothly than fcc planes (Fig. 15).

At high shear rates (De $>$ 0.4), we find a flow instability in PUT simulations of fcc systems. The instability arises because σ reaches a maximum value and begins to decrease with increasing De. It is interesting to note that the maximum value of the shear stress is very close to $\sigma_{\max}$. The instability is suppressed in PBT simulations, and may be suppressed by the solvent in experimental systems. Hydrodynamic forces must be included to determine stability of Couette flow, since their magnitude is increased by deviations from a Couette profile.

An important outstanding question is whether there are additional phase transitions within the solid region of the phase diagram. As shown in Figs. 11–13, there are definite structural changes as De increases. However, these changes appear to occur continuously. For example, the only discontinuities in the stress curves occur at the melting transition. There is a change in the derivative of the bcc stress near De = 0.15, but we have not identified any corresponding structural transition. Preliminary studies of $S(k)$ indicate that peak positions and intensities shift continuously with De. This is consistent with experimental studies [2,3], and is the subject of ongoing investigations [71].

The dimensionless shear rates studied here are higher than those which can be sustained in normal atomic solids. However, shear-induced melting may occur in recent experiments on nanometer thick films confined between atomically flat solid surfaces [33,73–75]. Solid walls can induce crystalline order in films at temperatures well above the corresponding bulk melting temperature [76]. In general, the induced order will not have the preferred alignment for shear, and the films will melt at much lower De than we have considered here. Simulations indicate that shear melting occurs when T is near the freezing point of the film [33,73]. At lower dimensionless temperatures, films may exhibit the flow instability found for fcc systems—shear localizes between a single pair of atomic layers [73]. Experimental determinations of the structural changes in these shearing films remain an open and exciting challenge.

ACKNOWLEDGMENTS

We thank B. J. Ackerson, G. S. Grest, K. Kremer, D. Ou-Yang, and P. A. Thompson for useful conversations and are indebted to P. M. Chaikin and H. M. Lindsay for their comments and the experimental data plotted in Figs. 1 and 7. Support from the National Science Foundation through Grant No. DMR 9110004 and the Pittsburgh Supercomputing Center is gratefully acknowledged.

[1] B. J. Ackerson and N. A. Clark, Phys. Rev. Lett. **46**, 123 (1981).
[2] B. J. Ackerson and N. A. Clark, Phys. Rev. A **30**, 906 (1984).
[3] B. J. Ackerson, J. B. Hayter, N. A. Clark, and L. Cotter, J. Chem. Phys. **84**, 2344 (1986).
[4] L. B. Chen, C. F. Zukoski, B. J. Ackerson, H. J. M. Hanley, G. C. Straty, J. Barker, and C. J. Glinka, Phys. Rev. Lett. **69**, 688 (1992).
[5] D. J. Evans, Phys. Rev. A **25**, 2788 (1982).
[6] J.-M. di Meglio, D. A. Weitz, and P. M. Chaikin, Phys. Rev. Lett. **58**, 136 (1987).
[7] P. Harrowell and M. Fixman, J. Chem. Phys. **87**, 4154 (1987).
[8] S. Ramaswamy and S. R. Renn, Phys. Rev. Lett. **56**, 945 (1986).
[9] B. Bagchi and D. Thirumalai, Phys. Rev. A **37**, 2530 (1988).
[10] R. L. Hoffman, Mater. Res. Soc. Bull. **16** (8), 32 (1991).
[11] S. Hess, Int. J. Thermophys. **6**, 657 (1985).
[12] R. L. Hoffman, Trans. Soc. Rheo. **16**, 155 (1972).
[13] R. L. Hoffman, J. Colloid Interface Sci. **46**, 491 (1974).
[14] M. J. Stevens, M. O. Robbins, and J. F. Belak, Phys. Rev. Lett. **66**, 3004 (1991).
[15] D. J. Evans, S. T. Chui, H. J. M. Hanley, and G. C. Straty, Phys. Rev. A **46**, 6731 (1992).
[16] J. J. Erpenbeck, Phys. Rev. Lett. A **52**, 1333 (1984).
[17] T. R. Kirkpatrick and J. C. Nieuwoudt, Phys. Rev. A **40**, 5238 (1989).
[18] J. F. Lutsko and J. W. Dufty, Phys. Rev. Lett. **57**, 2775 (1986).
[19] J. F. Lutsko, J. W. Dufty, and S. P. Das, Phys. Rev. A **39**, 1311 (1989).
[20] D. J. Evans and G. P. Morriss, Phys. Rev. Lett. **56**, 2172 (1986).
[21] L. V. Woodcock, Phys. Rev. Lett. **54**, 1513 (1985).
[22] D. M. Heyes, G. P. Morriss, and D. J. Evans, J. Chem. Phys. **83**, 4760 (1985).
[23] H. M. Laun, R. Bung, S. Hess, W. Loose, O. Hess, K. Hahn, E. Hädicke, R. Hingman, F. Schmidt, and P. Lindner, J. Rheol. **36**, 743 (1992).
[24] W. Loose and S. Hess, Rheol. Acta **28**, 91 (1989).

[25] W. Loose and G. Ciccotti, Phys. Rev. A **45**, 3859 (1992).
[26] W. Xue and G. S. Grest, Phys. Rev. A **40**, 1709 (1989).
[27] W. Xue and G. S. Grest, Phys. Rev. Lett. **64**, 419 (1990).
[28] A. Onuki and K. Kawasaki, Ann. Phys. (N.Y.) **121**, 456 (1979).
[29] P. G. de Gennes, Mol. Cryst. Liq. Cryst. **34**, 91 (1976).
[30] R. F. Bruinsma and C. R. Safinya, Phys. Rev. A **43**, 5377 (1991).
[31] P. D. Olmsted and P. M. Goldbart, Phys. Rev. A **46**, 4966 (1992).
[32] J.-P. Poirier, *Creep of Crystals* (Cambridge University Press, Cambridge, 1985).
[33] P. A. Thompson and M. O. Robbins, Science **250**, 792 (1990).
[34] E. J. Verwey and J. Overbeek, *Theory of Stability of Lyophobic Colloids* (Elsevier, Amsterdam, 1948).
[35] K. Kremer, M. O. Robbins, and G. S. Grest, Phys. Rev. Lett. **57**, 2694 (1986).
[36] M. O. Robbins, K. Kremer, and G. S. Grest, J. Chem. Phys. **88**, 3286 (1988).
[37] E. J. Meijer and D. Frenkel, J. Chem. Phys. **94**, 2269 (1991).
[38] B. B. Laird and D. M. Kroll, Phys. Rev. A **42**, 4810 (1990).
[39] D. W. Hone, S. Alexander, P. M. Chaikin, and P. A. Pincus, J. Chem. Phys. **79**, 1474 (1983).
[40] Y. Monovoukas and A. P. Gast, J. Colloid Interface Sci. **128**, 533 (1988).
[41] M. J. Stevens and M. O. Robbins, J. Chem. Phys. **98**, 2319 (1993).
[42] P. M. Chaikin *et al.*, in *Physics of Complex and Supermolecular Fluids* (Wiley-Interscience, New York, 1987), p. 65.
[43] H. M. Lindsay and P. M. Chaikin, J. Phys. (Paris) Suppl. **46**, C3 (1985).
[44] H. M. Lindsay, Ph.D. thesis, University of California at Los Angeles, 1988 (unpublished).
[45] H. J. M. Hanley, G. P. Morriss, T. R. Welberry, and D. J. Evans, Physica A **149**, 406 (1988).
[46] D. Brown and J. Clarke, Phys. Rev. A **34**, 2093 (1986).
[47] B. B. Derjaguin and L. Landau, Acta Phys. Chim. URSS **14**, 633 (1941).
[48] S. Alexander, P. M. Chaikin, P. Grant, G. J. Morales, P. Pincus, and D. W. Hone, J. Chem. Phys. **80**, 5776 (1984).
[49] M. J. Stevens, Ph.D. thesis, The Johns Hopkins University, 1991.
[50] M. O. Robbins, K. Kremer, and G. S. Grest, in *Phase Diagrams of Charge-Stabilized Colloidal Suspensions*, edited by N. Ise and I. Sogami (World Scientific, Singapore, 1988).
[51] H. M. Lindsay and P. M. Chaikin, J. Chem. Phys. **76**, 3774 (1982).
[52] When our work began the calculated melting line was higher and $Z^* = 450$ was consistent with the experimental line.
[53] D. J. Barber and R. Loudon, *An Introduction to the Properties of Condensed Matter* (Cambridge University Press, Cambridge, 1989).
[54] M. P. Allen and D. J. Tildesley, *Computer Simulation of Liquids* (Clarendon, Oxford, 1987).
[55] J. F. Joanny, J. Colloid Interface Sci. **71**, 622 (1979).
[56] D. J. Evans, in *Computer Modelling of Fluids, Polymers and Solids*, edited by C. Catlow, S. Parker, and M. Allen (Plenum, New York, 1990), p. 125.
[57] C. Cleveland, J. Chem. Phys. **89**, 4987 (1988).
[58] M. Parrinello and A. Rahman, J. Appl. Phys. **52**, 7182 (1981).
[59] C. W. Gear, *Numerical Initial Value Problems In Ordinary Differential Equations* (Prentice-Hall, Englewood Cliffs, NJ, 1971).
[60] S. Nose, J. Chem. Phys. **81**, 511 (1984).
[61] S. Y. Liem, D. Brown, and H. R. Clarke, Phys. Rev. A **45**, 3706 (1992).
[62] F. F. Abraham, Phys. Rep. **80**, 339 (1981).
[63] D. Thirumalai, J. Phys. Chem. **93**, 5637 (1989).
[64] J. C. Zahorchak, R. Kesavamoorthy, R. D. Coalson, and S. A. Asher, J. Chem. Phys. **96**, 6873 (1992).
[65] An exception occurs at very low shear rates in one recent experiment where individual crystallites rotate like ball bearings (Ref. [4]).
[66] In some orientations, the imposed periodic boundary conditions were not well-matched to the structure with the preferred alignment. This produced slight distortions of the final configuration.
[67] The temperature T cannot really be changed without also changing κ and the Yukawa potential. This may change the equilibrium phase.
[68] Values of c_{44}/G were obtained for the Yukawa potential with $Z^* = 625$, using effective medium theory to determine G from the other elastic constants [36]. The calculated ratio of the crystalline modulus c_{44} to the polycrystalline modulus G only varies from 1.8 to 1.7 as ρ_s increases, and a fixed ratio of 1.75 was used in scaling Fig. 7.
[69] L. M. Hood, D. J. Evans, and H. J. M. Hanley, J. Stat. Phys. **57**, 729 (1989).
[70] D. Ou-Yang (private communication).
[71] G. Magnusson, Jr., M. J. Stevens, and M. O. Robbins (unpublished).
[72] The time scale of shear-induced fluctuations is the time for the relative displacement of adjacent planes to reach a lattice constant. To limit the effect of thermal fluctuations in the microscopic pressure-stress tensor, we average the shear stress over much shorter times and calculated $\delta\sigma$ for these averaged quantities.
[73] P. A. Thompson, G. S. Grest, and M. O. Robbins, Phys. Rev. Lett. **68**, 3448 (1992).
[74] M. L. Gee, P. M. McGuiggan, and J. N. Israelachvili, J. Chem. Phys. **93**, 1895 (1990).
[75] J. V. Alsten and S. Granick, Langmuir **6**, 877 (1990).
[76] P. A. Thompson and M. O. Robbins, Phys. Rev. A **41**, 6830 (1990).